ARMA 23–434

Investigation of parameters affecting seismic potentials in a deep longwall mine

Khademian, Z.
NIOSH, Pittsburgh, PA, USA
Van Dyke, M. A.
NIOSH, Pittsburgh, PA, USA
Beale, J, Pilot Geophysical LLC and
Wickline, J., *Geologist*

ABSTRACT: Seismicity can be induced by rock failures or slips along geologic structures around mine workings. Depending on their intensity and proximity to the working area, seismic events may raise safety concerns in underground mining operations. However, the geological and mining parameters leading to destructive seismic events are poorly understood. Monitoring seismic events coupled with geomechanical modeling can be useful tools for understanding underlying mechanisms and main factors causing destructive seismic events. This paper reviews seismic events recorded in a deep longwall mine (>450 m) in Virginia and evaluates the geologic conditions that lead to areas with high seismic event activities (> 1 M_L) during mining of longwall panels. Two pseudo two-dimensional models of areas with high and low seismic event activities are constructed in 3DEC software. The variation in the energy content of elastic models is monitored, and potentially damaging events with compression-type and shear-type signatures are identified. The modeling results are compared with historic seismic data to evaluate the model performance in forecasting the seismic potential in each model. The results show the applicability of energy balance calculations for forecasting the approximate location and timing of destructive seismic events.

1. INTRODUCTION

One source of potential hazards for underground mining operations is mining-induced seismicity. Seismic events during mining are recognized to be violent failure in close proximity to the mining area. The violent failures can occur due to sudden crushing of rock in compression or sudden slip along preexisting weakness planes such as fault and dyke contacts. Deployment of seismic networks and recording the events during the operation has become one of the industry routines for managing risks associated with the seismicity. However, in most cases the main challenge is to find the link between geologic structures, mining parameters, and seismic activities. If no clear link is apparent, it is difficult to design effective proactive measures to reduce seismic potential in a mining design. To better understand the causal mechanism of mining-induced seismicity, seismological and rock mechanics' analyses need to be mutually investigated.

Following (Salamon, 1970), many studies have shown the energy budget consideration as the missing link between seismology and rock mechanics (Sears, 2009; Garvey, 2013; Khademian & Ozbay, 2018) One possible approach is to use numerical modeling to analyze the state of energy of the rock before and after mining. The occurrence and intensity of a seismic event can be recognized when there is a relatively significant release of energy in the system. However, the uncertainty in the required field data to perform such analyses has limited their applicability.

In 2022, the National Institute for Occupational Safety and Health (NIOSH) initiated a research project to investigate requirements for using models to estimate seismic potentials in a longwall setting. A series of tasks is defined to investigate step by step the level of complexity needed in a model for an acceptable estimate of seismic potentials in a longwall mine. The objective is to integrate the historic seismic data and experience in an energy-balance approach for understanding mechanisms of longwall-induced seismicity and estimating the potential for destructive seismic activities.

To this end, a review has been made on approaches for energy balance considerations. Simplified yet applicable methods have been selected to pave the way for a more complex modeling approach. The seismic database in a deep longwall mine in western Virginia is used for evaluating the employed methodologies. Two anomalous and subsequent events recorded in this mine in 2016 are selected to evaluate the underlying geologic and mining parameters that preceded them. The first event occurred on June 13, 2016, with a local magnitude of 2.5 M_L. The second event happened five days after with a magnitude of 3.7 M_L. To investigate the modeling capability in identifying potentials for anomalous events, a pseudo-2D, three-panel model was constructed in 3DEC (Itasca, 2016) at a cross section close to both events. The model includes panels 23, 24, 25 that are referred to as H-panels (panels with High seismic activity).

In order to compare the modeling results, another similar model is constructed in a region with few records of seismic events with less than 1-M_L magnitude. The model includes panels 19, 21, and 22 that are referred to as L-panels (panels with Low seismic activity). The three panels in each case are sequentially and gradually mined, and the energy budget and stress state are continuously evaluated for estimating the occurrence and intensity of seismic events during the mining simulation. This study paves the way for future investigation into the roles of various operational and geological parameters in the occurrence and intensity of damaging seismic events.

2. GEOLOGY DESCRIPTION

The longwall mine is operating within the Pocahontas #3 coal seam in western Virginia. The Pocahontas #3 coal seam is within the Pocahontas formation consisting of thick lens of sediments that consists of cyclothem intervals of sandstone, siltstone, shale, coal, and claystone. The lithologic sequence represents a paleogeographic transition from marine limestones during the Mississippian period to a barrier-bar with occasional swamp deposits from a continental setting depending on the sea level (Englund & Briggs, 1974). The study area is in southwestern Virginia within the Virginia overthrust belt, and the major fault impacting the mine is the Keen Mountain fault which is a strike-slip fault with compressional overthrusting (Molinda, 2003). The Keen Mountain fault does not directly impact the mine, but causes small synthetic thrust faults within the mining area with a minor offset of a maximum of 1.5 m.

The local mine roof lithology is shown in Fig. 1 and consists of a sequence of shales that vary from 0-7.6 m in thickness directly above the Pocahontas #3 coal seam. Above the initial shale is the first encounter sandstone, which has been named the Sandstone 1 (SS1) by the mine. The SS1 varies in thickness from 0–10.7 m and tends to be thin to medium bedded with shale or mica streaks especially when observed close to the shale below at the immediate roof. Above the SS1 is a thin shale parting that is typically 0 to 1.5-m thick. The shale parting covers the majority of the mining area, but in limited areas the parting is absent and the SS1 and the Sandstone 2 (SS2) compose one massive sandstone unit.

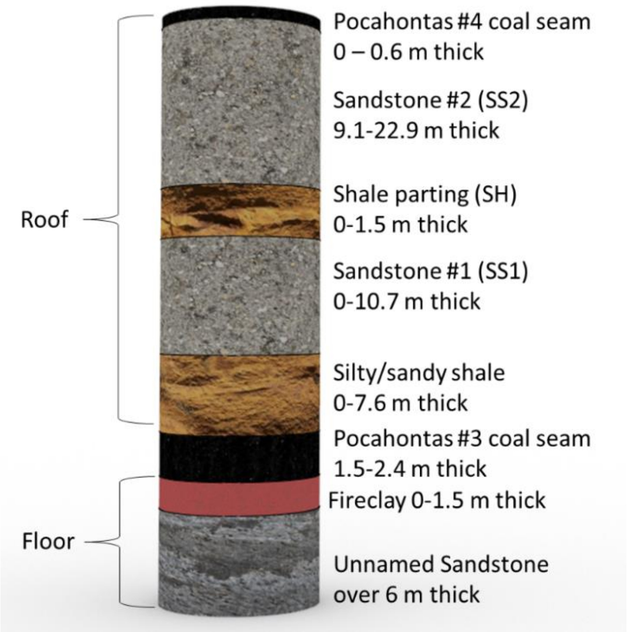

Fig. 1. Generalized stratigraphic column of the mine area.

The SS2 is generally the thicker and more massive sandstone in the immediate roof. The SS2 is cleaner than the SS1 and is thickly to massively bedded and varies from 9.1 to 22.8-m thick. The Pocahontas #4 coal seam is above the SS2 (Van Dyke, Su, & Wickline, 2018).

2.1. L-panels

The major note on the low seismic potential panels (panels 19, 21, 22) is that the overburden is relatively shallow due to a valley. The overburden is between 400–500 m. The SS1 and SS2 sandstones are thick in this area, between 21–24 m with the exception of panel 19, which only has a thickness of 9 m. The same can be seen with the caving height, which is low between panels 20–22 (2.5–4 m) and high in panel 19 at 7.6 m.

2.2. H-panels

In the cross section covering the high potential panels (panels 23–25), the overburden is thicker and ranges within 578–638 m. Compared to L-panels, the sandstones are also thicker in this area ranging from 24–43 m. The caving height is estimated to be 4.5 m or less.

3. SEISMIC HISTORY

3.1. Event distribution

An examination of event distribution, within a roughly 300-m span from north to south, extending across six mined panels in two districts from west to east, shows a stark contrast between seismicity levels from the western half (L-panels) to the eastern half (H-panels) of this zone (Fig. 2).

The L-panels include the latest-mined panel from a previous district and the earliest-mined two panels from the subsequent district, and the H-panels include the latest-mined three panels from the subsequent district.

The seismicity level in the eastern half is significantly higher than the western half, with nearly double the number of events above magnitude 0, nine events above magnitude 1, compared to none in the western half, as well as one magnitude 2.5-M_L event and one magnitude 3.7-M_L event. Both large events occurred during mining panel 25. From the surface seismic stations shown in Fig. 2, 3.7-M_L event occurred in the tailgate of panel 24 and 2.5-M_L event occurred in tailgate of panel 25. Some mining-geometry related factors contribute towards this distribution, particularly the fact that the earliest-mined panels in a district consistently exhibit lower levels of seismicity than the later-mined panels of the same district.

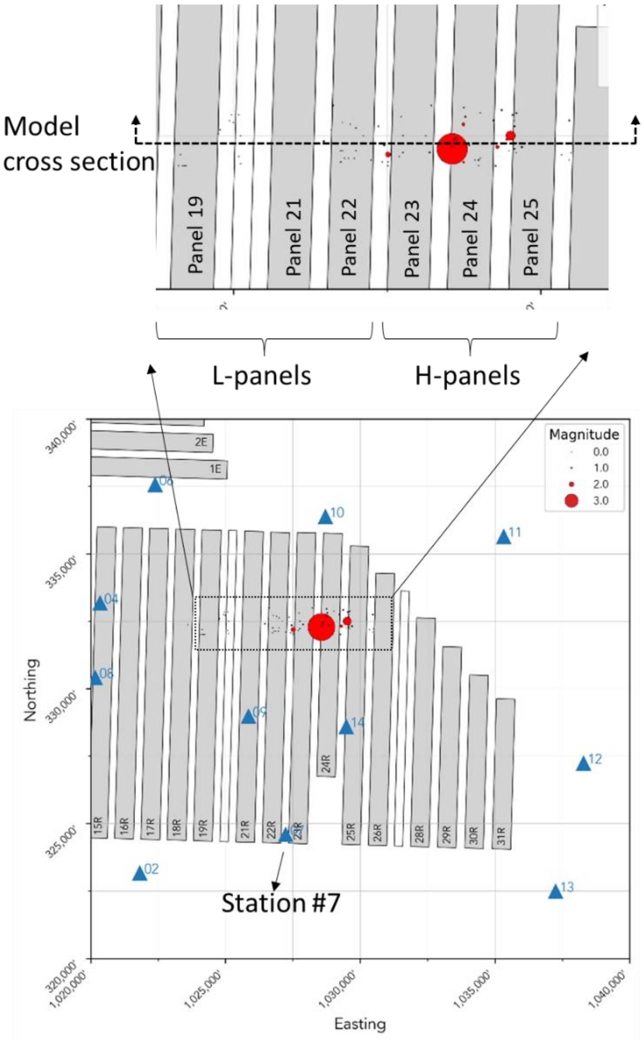

Fig. 2. Plan view of panels in the area of interest along with the surface station location.

However, the latest-mined panel of the previous district was included in the L-panels, and it showed virtually no seismicity, indicating that other factors must be involved to produce such a discrepancy in seismicity levels.

3.2. *Non-isotropic element of source mechanism*

The vast majority of the seismic events at the mine exhibit dilatational first motions at all surface recording stations, indicating that the source is essentially isotropic and consistent with a downward displacement of rock mass. Some events, particularly within the set of events larger than 1 M_L, exhibit a small compressional first motion within a range of azimuths, indicating a small slip on a plane of failure associated with the event, and occurring at its initiation time. This non-isotropic contribution to the energy release varies in size for different events but is typically small compared to the overall size of the event. The two large events which occurred in July 2016 in close proximity to each other both exhibited a small amount of compressional first motion at two recording stations located to the south of the events. Fig. 3 shows the ground displacements associated with the 2.5-M_L event recorded at station #7, in the south of the event.

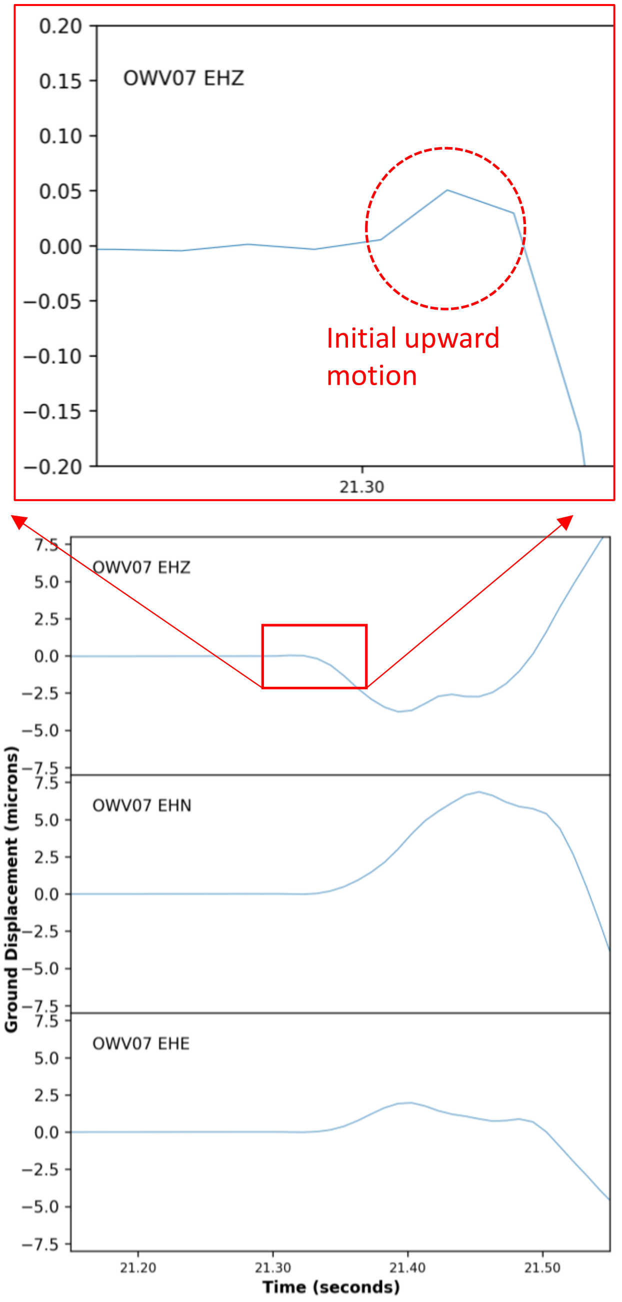

Fig. 3. Ground displacements recorded at station #7 in EHZ, EHN, and EHE components for the 2.5-M_L event

For the 2.5-M_L event, the amplitude of the upward first motion (measured on corrected vertical components as shown in zoomed view in Fig. 5) is no more than a few percent of the total downward motion of the main pulse of the primary wave. The non-isotropic contribution is even less significant on the larger 3.7-M_L event as shown in Fig. 4.

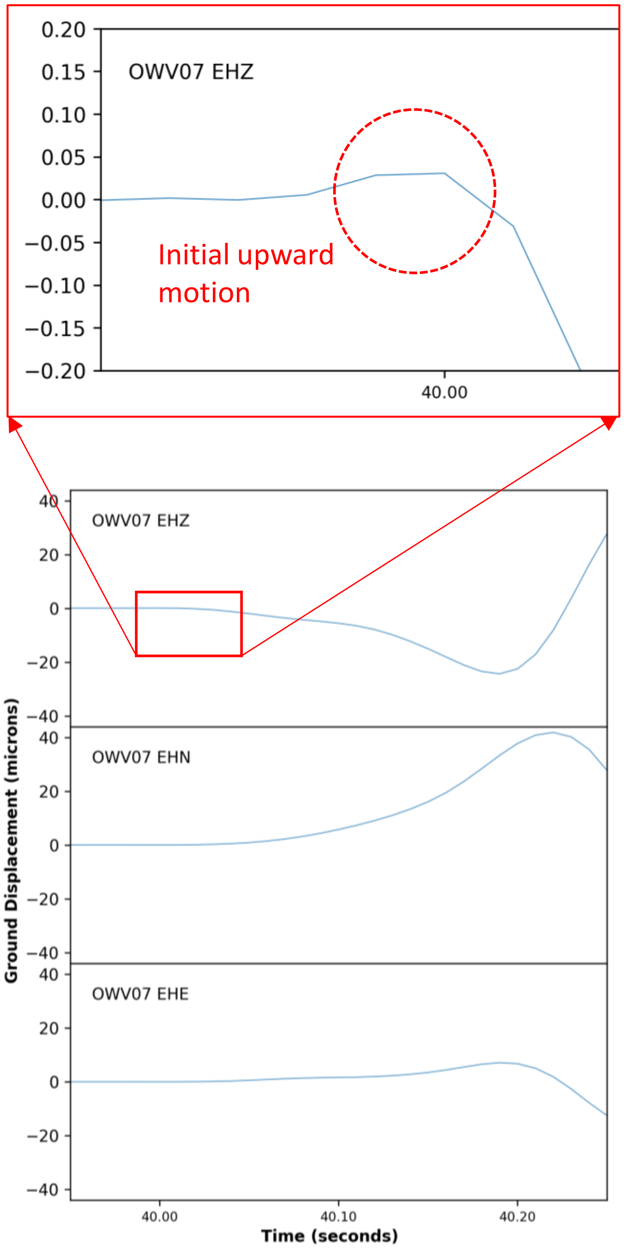

Fig. 4. Ground displacements recorded at station #7 in EHZ, EHN, and EHE components for the 3.7-M_L event

Overall, the two events appear to consist largely of isotropic energy release, but these small complexities indicate the presence of at least a small contribution of a non-isotropic mechanism to the overall event. This probably indicates that slip on planes of failure has triggered the events, but more data and analyses are required to calculate the seismic moment tensor for each event and certainly discuss the focal mechanisms.

4. METHODOLOGY

The goal is to shed some light on the factors contributing to the occurrence and intensity of seismic events. For studying mining-induced seismic events, energy balance equations are a possible link amongst rock failure mechanics, main geology features, and seismology.

When mining underground, at each stage of development, energy becomes available from the work (W) done by external forces, working on the convergence of the opening, and the strain energy that was stored in the mined-out area U_m. The mechanical equilibrium is regained if this available energy $(W + U_m)$ is dissipated through storing strain energy in the surrounding rock (U_c), consuming energy by inelastic deformation of rockmass (W_p), and releasing energy as radiated seismic energy (W_k). The following equation represents energy budget changes by mining process (Salamon 1970).

$$W + U_m = W_p + U_c + W_k \tag{1}$$

If available energy $(W + U_m)$ is more than $W_p + U_c$, energy has to be released dynamically with a signature of a seismic event with magnitudes depending on the excess energy of W_k.

The seismic event can be the result of a sudden release of compressive stress through crushing of the rock with a dilation signal or a sudden release of shear stress through slip along discontinuities or intact rock with a standard 4-quadrant fault plane signature.

Many studies investigated the release of energy and potential for seismic activities through fully solving the energy balance at each stage of mining and calculating W_k (Garvey, 2013; Khademian & Ozbay, 2018). However, such an approach requires calculation of W_p that needs complex constitutive models to simulate strain-weakening rock failure and slip-weakening sliding through pre-existing discontinuities and main geologic features. The main uncertainty in such modeling exercise is the weakening response (post-failure) of rockmass and discontinuities under mining-induced stress. In order to provide a benchmark for such complex mechanical models, this paper makes simplifying assumptions and uses indirect indicators of W_k to assess seismic potentials in a mining setup.

Assuming rock is perfectly elastic and mining advances gradually, energy available in the system is fully stored as U_c in Equation 1. The first question is how to decide on the occurrence of an event in an elastic model. The occurrence of a seismic event depends on the stress level, post-peak response of rock, interface frictional properties, and loading system stiffnesses. In an elastic system, the level of stress compared to the rock strength is probably a simple yet practical indication of occurrence potentials. However, it should be noted that without a finite stress drop, there is no potential for violent slip along discontinuities. Similarly, violent crushing of rock volume is impossible if the rock fails with no sudden post-failure weakening or loss in strength.

The second question is how to estimate the intensity of seismic events in an elastic model. Studies showed that the initial state of strain energy and its variation with mining can be an indicator of seismic event intensity (Mitri, Tang, Comeau, & Mohammed, 1999). In other words, once conditions for seismic failure are met, the higher budget of energy available in the system ($\mathrm{W} + \mathrm{U}_m$) may lead to the higher level of W_k. In an elastic system U_c is a measure of the available energy.

4.1. Compressive-type events

(Castro, Bewick, & Carter, 2012) and (Martin, Kaiser, & Mccreath, 1999) proposed a deviatoric stress approach to identify zones with the potential for rock mass damage initiation around a deep opening, given as:

$$(\sigma_1 - \sigma_3) = 0.4 \text{ to } 0.5 \ \ \mathrm{UCS} \qquad (2)$$

(Castro et al., 2012) defined a ratio of 0.6 to 0.7 for moderate potential and > 0.7 for major potential of seismic events. Following the same approach, zones prone to high-energy events, referred to as seismogenic zones, are identified where

$$\frac{(\sigma_1 - \sigma_3)}{\mathrm{UCS}} > 0.7 \qquad (3)$$

is satisfied. Then, strain energy is calculated within the seismogenic zone. Thus, each model can be represented by the volume of zones satisfying inequality (3) and the respective strain energy variations of U_c. Then, U_c can be calculated as the difference between the initial (pre-mining) and current state of Strain Energy Density (SED) given as:

$$SED = \sum \frac{1}{2E}[\sigma_1^2 + \sigma_2^2 + \sigma_3^2 - 2\nu(\sigma_1\sigma_2 + \sigma_1\sigma_3 + \sigma_2\sigma_3)] \qquad (4)$$

where σ_1, σ_2, σ_3 are the principal stresses in each zone in the model; ν and E are the Poison ratio and Young's modulus of the rock. To calculate total strain energy change in each zone, SED should be multiplied by the zone volume.

4.2. Shear-type events

Occurrence of shear-type seismic events induced by mining activities are frequently reported with evidence ranging from pure shear-type moment tensors to a combination of shear and compressive-type events to the clear trace of earthquake-type rupture exposed on the surface (Ryder, 1988).

For the shear-type events, W_p in Equation 1 is the result of frictional sliding along discontinuities. Initiation and propagation of rupture depends on the stress level, friction properties, post-peak weakening of the discontinuity, and the loading system stiffnesses (Khademian & Ozbay, 2018). Shear stress that drives the slip and the frictional properties of the faults are the most important parameters. Frictional resistance to slip τ_s is commonly found to increase linearly with the normal stress σ_n, given as

$$\tau_s = \mathrm{C} + \sigma_\mathrm{n} \tan(\varphi_s) \qquad (5)$$

where C is the cohesion between discontinuity plates and φ_s is the friction angle. Most researchers in earthquake theory agree on the concept of dynamic friction, φ_d, a reduced level of friction resistance that emerges once slip occurs, given as

$$\tau_d = \sigma_\mathrm{n} \tan(\varphi_d) \qquad (6)$$

Under dynamic conditions, cohesion is said to be negligible, and friction can be reduced due to many reasons such as shearing macroscopic or microscopic asperities, but here we assume lack of cohesion is the only difference between τ_s and τ_d.

The prevailing shear stress on the fault is another important factor because W_k cannot emerge if the level of stress is lower than the dynamic strength of the fault. Following this logic, Ryder (1988) defined Excess Shear Stress (ESS):

ESS=Prevailing shear stress prior to slip – dynamic shear strength

as an indicator for the seismic potential of a discontinuity. This concept is explained in Fig. 5 where static and dynamic strength of a discontinuity are shown. The red line is the prevailing shear stress that meets with the static friction curves at a few points and could lead to rupture initiation. As shown in this figure, the stress on the plane can vary in different forms, and thus ESS varies along the plane of weakness. In summary, ESS can be thought of as the net force available to drive a shear-type seismic event once rupture has initiated.

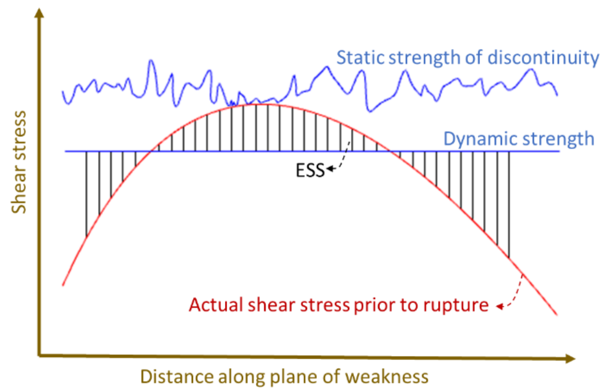

Fig. 5. Shear stress and strength conditions along a plane of weakness [After Ryder, 1988]

Careful laboratory experiments and field calibration are needed to define the range of ESS that can lead to high seismic potentials, but in the meantime, the following suggested representative values (Ryder, 1988) are used in this paper:

ESS <0: No event is possible.
ESS <5 MPa: Seismic activity is unlikely.
ESS >15MPa: Destructive seismic events are likely.

The average ESS is calculated along each plane of weakness in the model. The weakness bedding plane with ESS>5 MPa is referred to as seismogenic planes. ESS is then averaged over this area of elevated shear stress. For estimating the intensity of a shear-type seismic event, it is assumed that ESS is distributed evenly over the seismogenic area. From Ryder (1988), for a uniformly distributed ESS, seismic moment can be calculated from:

$$M_o = 2.25\,\tau_e\,\mathrm{a}^2\,\mathrm{L} \qquad (7)$$

where τ_e is the average ESS and a is the half-width of ESS contour, and L is the strike. W_k can then be estimated from

$$\mathrm{W}_k = \frac{M_o \tau_e}{2G} \qquad (8)$$

where G is the shear modulus of the surrounding rock. Table 1 lists a summary of the Methodology section, showing the criteria for identifying a seismic event and its intensity.

Table 1. Criteria for identifying the occurrence and intensity of seismic events in elastic medium

Event type	Shear	Compressive
Event occurrence criteria	ESS > 5 MPa	$\frac{(\sigma_1 - \sigma_3)}{\mathrm{UCS}} > 0.7$
Event intensity if occurring	W_k in Eq. 8	U_c in Eq. 4

The methodologies explained here are used for understanding seismic potential in any given model in the next sections.

5. MODEL DESCRIPTION

Two separate pseudo-2D models in 3DEC are generated. The surface topography follows the cross section in Fig. 6. Although the lateral variations in the thickness of the stratigraphic layers could be modeled, a generalized stratigraphic column is used for each model to simplify the geometry. Fig. 6 shows the two generalized columns used to generate each model with their field-scale mechanical properties and friction angle of the bedding planes separating each layer. A portion of the 3DEC model geometry is also shown for L-panels that include panels 19, 21, and 22 along with the H-panels that include panels 23, 24, and 25.

The model is brought to equilibrium under in-situ stresses with elastic materials, but interfaces are given friction angles listed in Fig. 6. After reaching equilibrium, the contacts are given very high cohesion values to prevent any sliding along the interfaces between layers. The tensile strength of the contacts is, however, kept at an average value of 0.5 MPa to allow the separation of the immediate roof. All development works are mined first followed by mining the panels according to the operational schedule. The mining process is simulated using a load-relaxation technique where after removing the materials, the traction along the removed boundaries is gradually reduced to zero. Thus, a gradual face advance is simulated in this pseudo-2D modeling environment. The load reduction for each stage occurs in 100 steps. The SED and ESS values are recorded for each layer and their interfaces, respectively. The change in the SED compared to the pre-mining state of the model is averaged over the seismogenic volume of rock, zones which meet $\frac{(\sigma_1 - \sigma_3)}{\mathrm{UCS}} > 0.7$. The sum of the total change in the strain energy of the seismogenic volume of the rock is also recorded. ESS values are also averaged over the area of

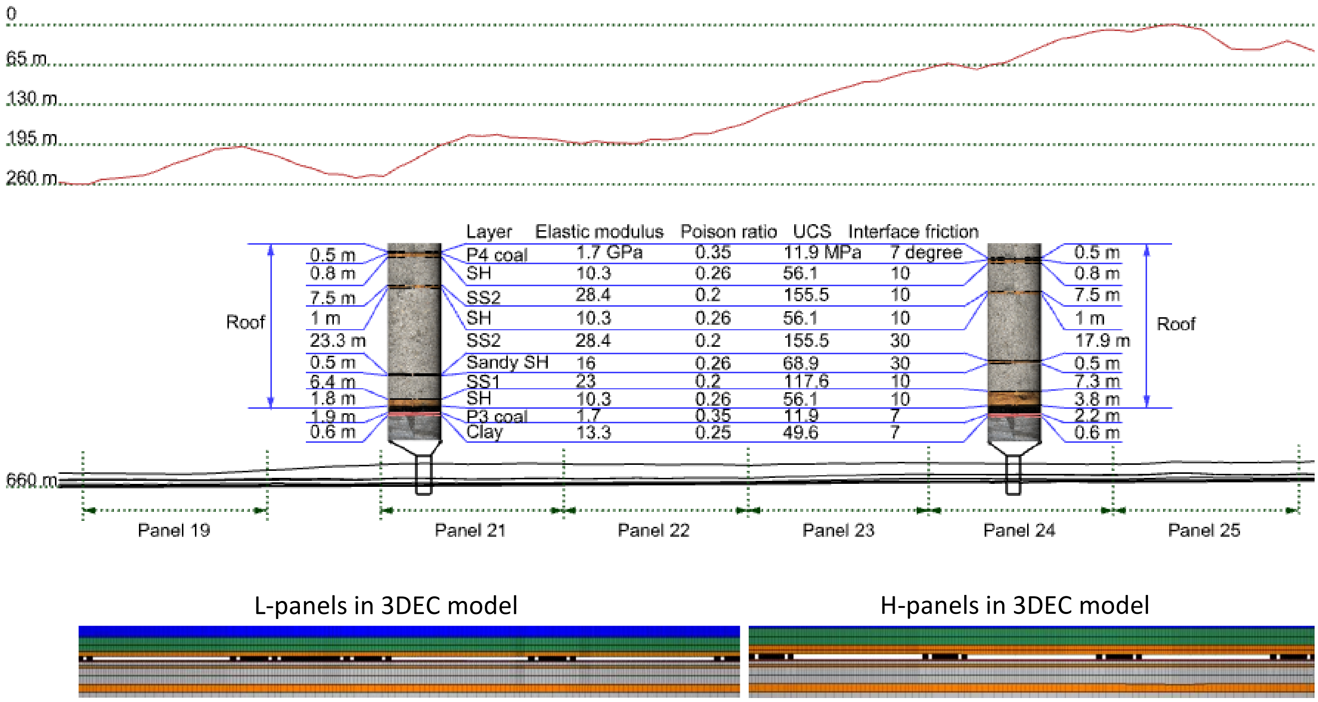

Layer	Elastic modulus	Poison ratio	UCS	Interface friction
P4 coal	1.7 GPa	0.35	11.9 MPa	7 degree
SH	10.3	0.26	56.1	10
SS2	28.4	0.2	155.5	10
SH	10.3	0.26	56.1	10
SS2	28.4	0.2	155.5	30
Sandy SH	16	0.26	68.9	30
SS1	23	0.2	117.6	10
SH	10.3	0.26	56.1	10
P3 coal	1.7	0.35	11.9	7
Clay	13.3	0.25	49.6	7

Fig. 6. Lithologies and surface topography used to model L-Panels and H-Panels.

the seismogenic bedding planes, which are the contacts that exhibit ESS>5MPa. The results are summarized in the following Results section.

6. RESULTS

The modeling results are discussed here in two subsections. First, the potential for compressive-type events is evaluated by comparing SED values for each model. Then, the potential for shear-type events is studied by looking at the ESS values and the calculated radiated seismic energy.

6.1. SED change in seismogenic strata

Fig. 7 shows how SED increases over time as the mining advances from the first panels to the third panels in both models. In Fig. 7, each layer in the roof is shown with a positive number starting from the immediate shale roof being 1. The layers located in the floor are shown with negative numbers starting from the fireclay floor being -1. From Fig. 7a, the immediate roof, coal seam, immediate floor, and shale floor start showing limited signs of seismic activities from the beginning of the first-panel mining. During the second-panel mining, the sandstone floor joins the group of the seismogenic layers with SED change that exceeds the previous layers except the coal seam. During the third-panel mining, the main sandstone roof SS1 – shown as 2 (roof-SS1) in Fig. 7 – becomes seismogenic. Fig. 8 shows the location where the rise in the stress level happens and thus SS1 becomes seismogenic according to inequality (3).

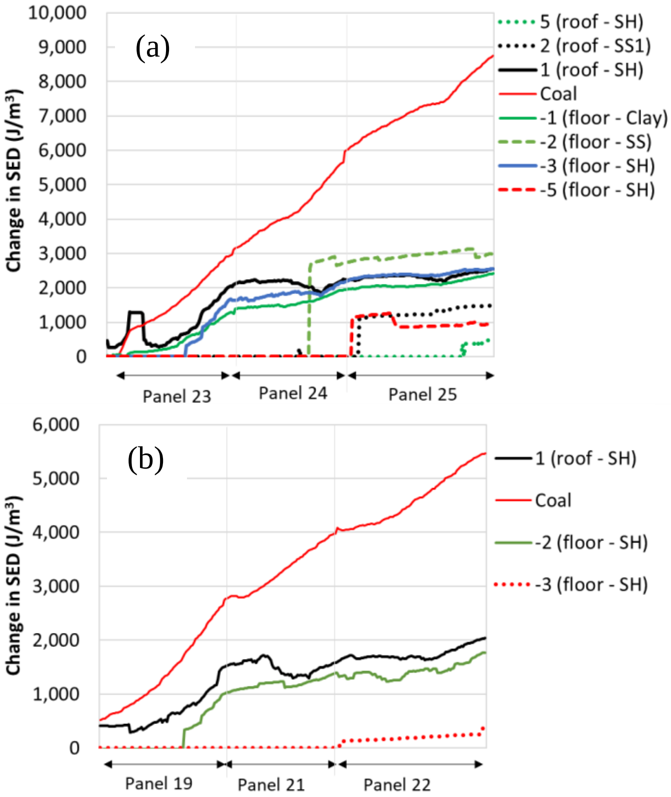

Fig. 7 Change in the strain energy density of seismogenic layers versus time for (a) H-panels and (b) L-panels during mining. The solid curves show the layers that show seismic potential starting from the first-panel mining. The dashed curves show the layers that become seismogenic during the second panel. The dotted curves represent the layers that become seismically active during the third panel mining.

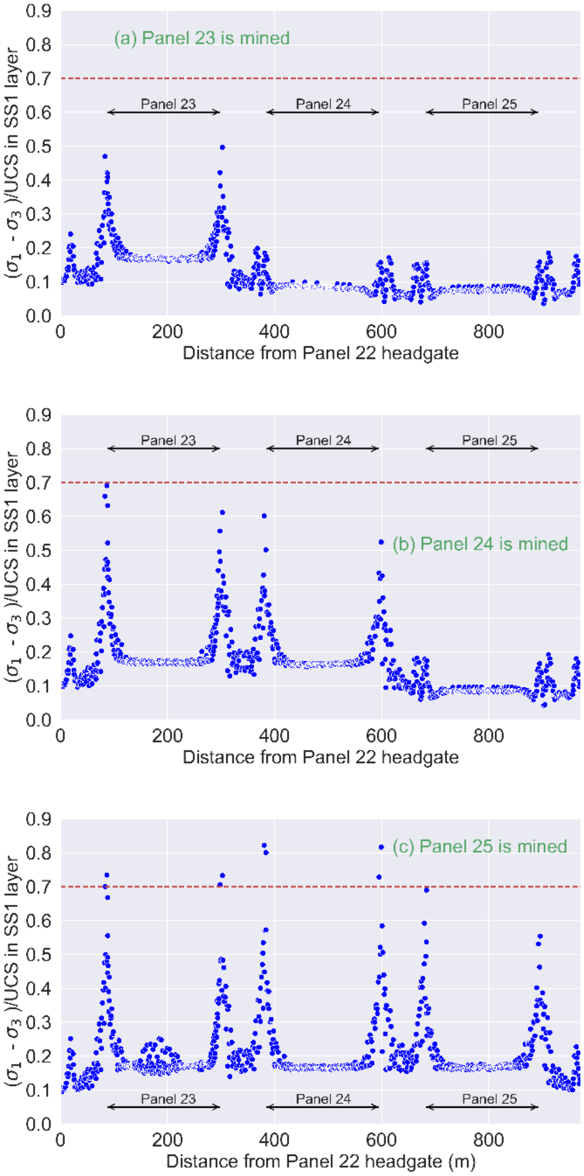

Fig. 8. Change in the stress level of SS1 unit above the immediate shale roof (a) after first panel is mined, (b) after the second panel is mined, and (c) after the third panel is completed.

In Fig. 8, stress level in the form of $(\sigma_1 - \sigma_3)/UCS$ is plotted across the panels in the SS1 unit, shown as 2 (roof-SS1) in Fig. 7. Fig. 8a shows the stress level after completion of the first panel in the model, panel 23. The stress level reaches 0.5 in the headgate and tailgate of this panel. Fig. 8b shows the stress result in SS1 after the second panel, panel 24, is mined. $(\sigma_1 - \sigma_3)/UCS$ reaches 0.7 in the headgate of the first panel, making SS1 in this area seismogenic. When the third panel, panel 25 is completed, $(\sigma_1 - \sigma_3)/UCS$ goes beyond the threshold of 0.7 in the tailgate and headgate entries of the first and second panels. Similar results are observed for the shale units in the roof and floor.

Comparing SED results with the discussion in Section 3.1, the location of events in Fig. 2 implies that the 3.7-M_L and 2.5-M_L events could have occurred in the main roof or floor layers. This is because based on Fig. 7 and Fig. 8, the roof and floor strata in the tailgate and headgate entries of panels 23 and 24 become seismogenic during the mining of panel 25. This agrees with the timing and location of the 3.7-M_L and 2.5-M_L events.

However, the maximum SED change occurs in the coal seam with a value of 8,800 J/m^3. Thus, the seismicity happened in H-panels could also be related to the Pocahontas #3 coal pillars. However, the growth of SED in the coal seam is steady as opposed to that in the roof and floor. Besides, yield pillars are designed to consume the available energy in the mine that cannot be considered in an elastic model.

In contrast, for the L-panels in Fig. 7b, only the immediate roof and floor become seismogenic during the last panel mining. The maximum SED also belongs to the coal seam with about 5,500 J/m^3. To compare the seismic potential in each model, the total change in the strain energy can be considered.

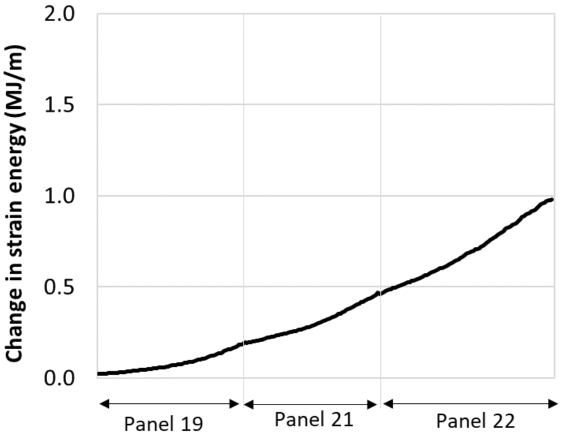

Fig. 9 shows the sum of the SED values in each seismogenic zone multiplied by their volume.

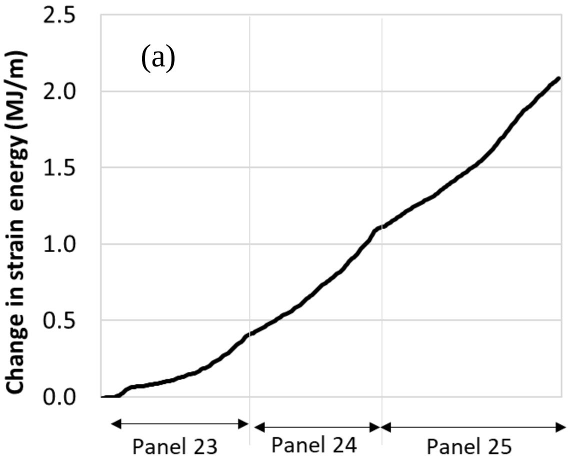

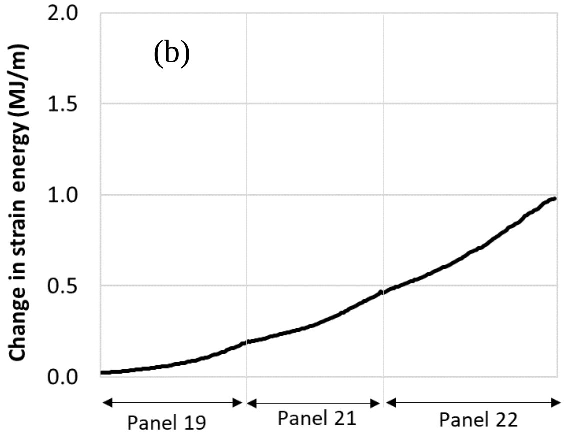

Fig. 9. Total change in the strain energy of the seismogenic layers per panel length over time from the pre-mining state of the model for (a) H-panels and (b) L-panels during mining.

Comparing the results in Fig. 9a and Fig. 9b, it is evident that the magnitude of the total strain energy of H-panels after the completion of the third panel is almost two times that of the L-panels. The difference between the strain energy is about 1 Megajoules per unit length of the panel (MJ/m). Assuming the strain energy changes due to mining is representative of seismic potential, the modeling results show higher potentials for seismic activities in H-panels, which is in agreement with the historic seismic data in Section 3.

6.2. *ESS in seismogenic bedding planes*

Excess shear stress along interfaces is plotted in Fig. 10a and Fig. 10b during mining the H-panels and L-panels, respectively. In Fig. 10, each bedding plane in the roof is shown with a positive number starting from the shale-coal interface in the roof being 1. Similarly, each bedding plane in the floor is shown with a negative number starting from the coal-clay interface in the roof being -1. The bedding planes between the coal and immediate roof and floor become seismogenic during the development stages. This is because the high shear stress values developed in the roof and floor of the gateroad entries. The bedding plane between the immediate shale roof and main sandstone roof SS1 becomes seismically active at the end of the first-panel mining. The wide variation in the SS1-SH bedding planes is due to the separation of the immediate shale from SS1 after the panel is completed.

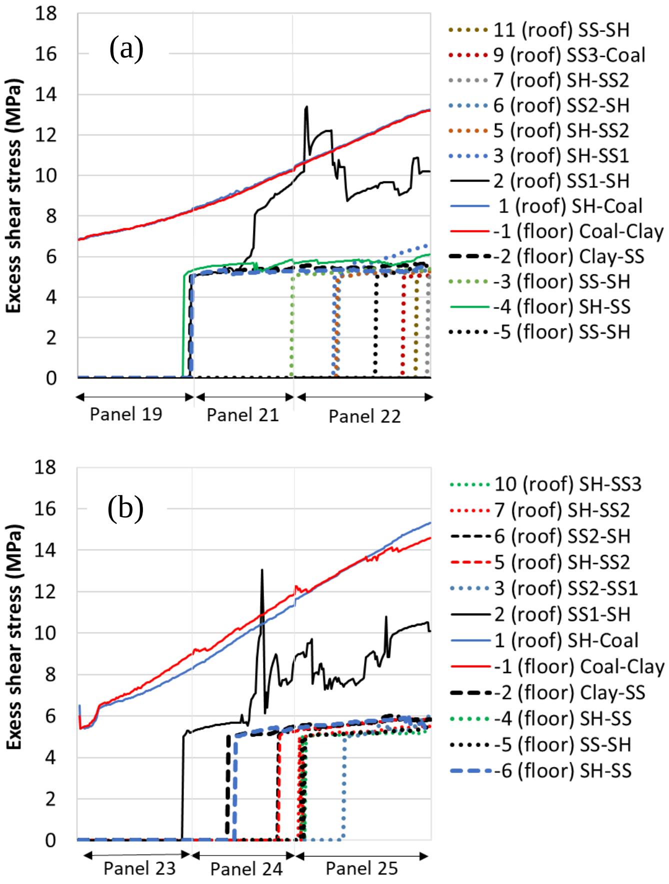

Fig. 10. Excess shear stress along seismogenic bedding planes versus time for (a) H-panels and (b) L-panels. The solid curves show the bedding planes that show seismic potential starting from the first-panel mining. The dashed curves show the planes that become seismogenic during the second-panel mining. The dotted curves represent the planes that become seismically active during the third-panel mining.

Fig. 11 shows the location of the ESS values across the panels in the shale-SS1 interface. Similar to the results for SED in Fig. 8, the rise in ESS happens in the panels mined before the active panel. Thus, when panel 25 is mined, there happens a jump in ESS around the tailgate and headgate entries of panel 24. This observation is in line with the seismic records as shown in Fig. 2 and discussed in Section 3.

The ESS variations in Fig. 10a and Fig. 10b seem close, so both L-panels and H-panels could have similar potential for seismic activities if the seismic intensity is to be neglected.

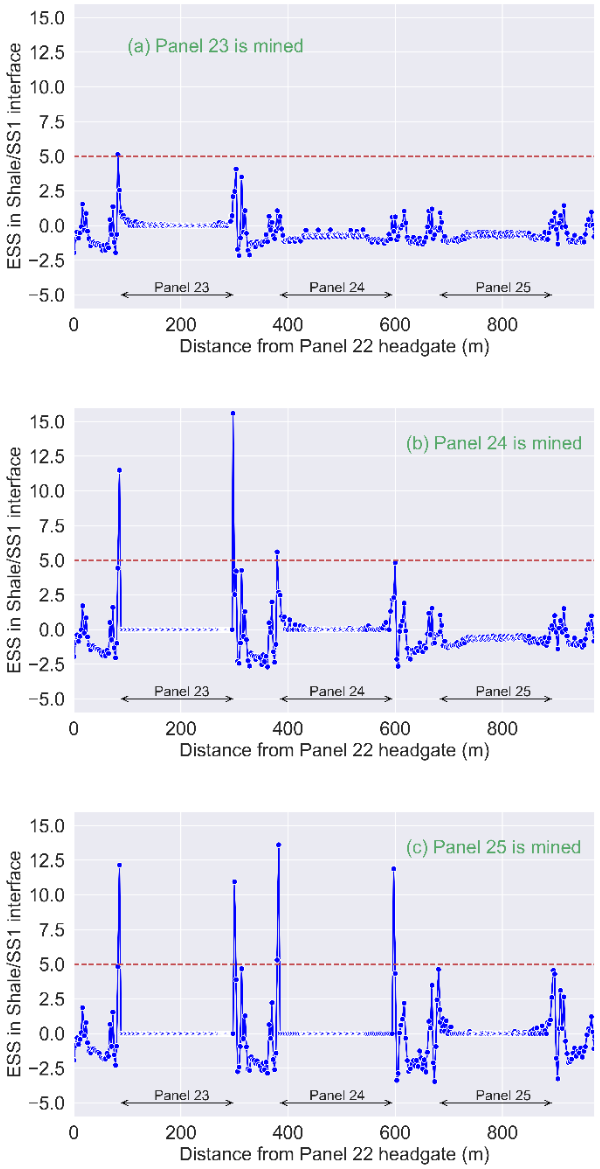

Fig. 11. Variation in ESS values along the interface between immediate roof and SS1 for (a) panel 23 is completed, (b) panel 24 is completed, and (c) panel 25 is mined.

Fig. 12 shows the variation of the seismic intensity by summing total radiated energy W_k from all seismogenic bedding planes in L-panels and H-panels. W_k is calculated from Equation 8.

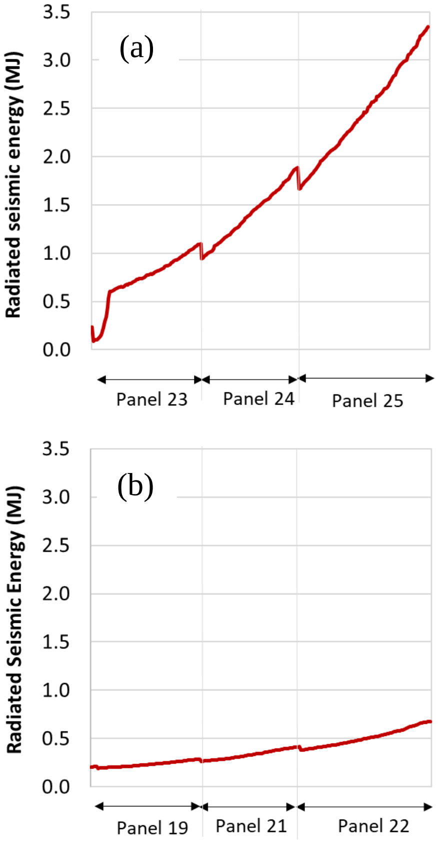

Fig. 12. Sum of the radiated seismic energy calculated from ESS on each seismogenic bedding planes for (a) H-panels and (b) L-panels.

At the beginning of each panel, there is a drop in the energy because of the loss of the bedding plane due to mining the panel, but the trend is increasing over the course of mining. A comparison between Fig. 12a and Fig. 12b shows a drop in W_k from 3.3 MJ in the H-panels to 0.7 MJ in the L-panels. While ESS is closed for both cases, the significant difference comes from the area of the seismogenic bedding planes. In H-panels, a wider area of planes becomes seismogenic and then contributes to the W_k magnitude.

7. DISCUSSION

From Section 3 and an initial evaluation of first motions, it was expected that the potential for both compressive-type and shear-type events would be observed, especially in the H-panel models. Also, overall, less seismic potential was expected from L-panels compared to H-panels. Fig. 9 confirmed that the energy available for compressive-type seismic activities in H-panels is almost twice that of L-panels. However, from the modeling results, it is not clear what portion of this energy would be released dynamically as W_k. From the seismic history during mining of L-panels, one could conclude the available energy has been consumed by the plastic work due to the rock mass deformation and fracturing.

Fig. 12 confirmed the potential for the shear-type events in both L-panels and H-panels. The radiated seismic energy for the latter is almost four times the former. This signifies the possibility of bedding planes as a contributor to the double-couple signature in the first motion analyses in Section 3. However, the magnitude of W_k in Fig. 12 for H-panels are more than the strain energy available for compressive-type events in Fig. 9. This can be related to the fact that the models generated and discussed here are pseudo-2D that means the energy values are in the unit of Joule per unit length in the third (in-plane) direction. The extend of seismogenic layers in in-plane direction defines the absolute values of energy available and released for each type of event. In this case, the shear-type events may be more local depending on the geology and stress variations in in-plane direction compared to the compressive events. This can be also related to the fact that ESS as a seismic potential indicator is over-conservative. This is because from all the seismogenic bedding planes with the potential for violent slip, a few may rupture and thus prevent the shear stress elevation in other planes. Therefore, a further modeling exercise is recommended with more realistic bedding-plane frictional properties and rock failure response to understand the contribution of such phenomena. The results here provided a benchmark for comparison.

8. CONCLUSION

We investigated a simple yet practical approach to estimate the seismic potential for a given mining setting. Two regions with distinctive potential for seismic activity according to the historic data were selected in a longwall mine in western Virginia. The results showed that for the compressive-type seismic events 110% more energy is available in the region with high seismic activities. The radiated seismic energy estimated by the model also showed a distinct difference of 391% in the potential for shear-type seismic events along bedding planes in the region with historically high seismic activities. The rise in the SED and ESS values occurred in the tailgate and headgate of the second panel when the third panel was being mined, which agrees with the location and timing of the 3.7-M_L and 2.5-M_L seismic events that occurred in 2016. The results showed the usefulness of ESS and SED as measures of seismic potentials. This provided a solid ground for future studies using more complex energy-balance equations and constitutive models, which may allow estimating seismic event intensity in numerical models of underground mines.

9. REFERENCES

Castro, L. B., Bewick, R., & Carter, T. (2012). *An overview of numerical modelling applied to deep mining*.

Englund, K. J., & Briggs, G. (1974). Sandstone Distribution Patterns in the Pocahontas Formation of Southwest Virginia and Southern West Virginia. In *Carboniferous of the Southeastern United States* (Vol. 148, pp. 0): Geological Society of America.

Garvey, R. J. (2013). Study of unstable rock failures using finite difference and discrete element methods, A. In: Colorado School of Mines. Arthur Lakes Library.

Itasca. (2016). 3DEC user mannual: Itasca Consulting Group. Retrieved from https://www.itascacg.com/

Khademian, Z., & Ozbay, U. (2018). Computational framework for simulating rock burst in shear and compression. *International Journal of Rock Mechanics and Mining Sciences, 110*, 279-290. doi:https://doi.org/10.1016/j.ijrmms.2018.06.022

Martin, C. D., Kaiser, P. K., & Mccreath, D. R. (1999). Hoek-Brown parameters for predicting the depth of brittle failure around tunnels. *Canadian Geotechnical Journal, 36*, 136-151.

Mitri, H. S., Tang, B., Comeau, W., & Mohammed, M. M. (1999). *3-Dimensional Modelling of Mining Induced Seismic And Strain Energy Parameters*. Paper presented at the 9th ISRM Congress.

Molinda, G. M. (2003). *Geologic Hazards and Roof Stability in Coal Mines*. Retrieved from

Ryder, J. A. (1988). Excess shear stress in the assessment of geologically hazardous situations. *Journal of The South African Institute of Mining and Metallurgy, 88*, 27-39.

Salamon, M. D. G. (1970). Stability, instability and design of pillar workings. *International Journal of Rock Mechanics and Mining Sciences & Geomechanics Abstracts, 7*(6), 613-631. doi:https://doi.org/10.1016/0148-9062(70)90022-7

Sears, M. M. (2009). *Implementing energy release rate calculations into the LaModel program*.

Van Dyke, M. A., Su, W. H., & Wickline, J. (2018). Evaluation of seismic potential in a longwall mine with massive sandstone roof under deep overburden. *International Journal of Mining Science and Technology, 28*(1), 115-119. doi:https://doi.org/10.1016/j.ijmst.2017.12.014